



Cite this: *J. Mater. Chem. C*, 2023, **11**, 15443

Superhydrophobic coating with a micro- and nano-sized MnO₂/PDMS composite structure for passive anti-icing/active de-icing and photothermal applications†

Jialun Li,^a Fei Yu,^a Yi Jiang,^b Liying Wang,^b Yaodong Liu,^a Xijia Yang,^a Xuesong Li^{*a} and Wei Lü^{*ac}

The formation and accumulation of ice can induce serious economic damage. Eco-friendly anti-icing/de-icing surfaces have been developed to address these problems. Superhydrophobic photothermal coatings have received significant attention in recent years, but an anti-icing/de-icing coating which is robust and facile to prepare is highly desired. Herein, a fluorine-free MnO₂/PDMS superhydrophobic coating was prepared using a facile spraying method. The excellent superhydrophobicity (water contact angle of 162.3°) and good self-cleaning properties were due to the surface microstructure of micron/nano-scale MnO₂ with the “lotus leaf effect”, while the coating was able to maintain efficient photothermal properties over time, with excellent passive anti-icing and active de-icing properties. In terms of mechanical durability, it was subjected to severe tests (sandpaper abrasion, tape-peeling, sand-washing, sonic treatment) and maintained good robustness. Based on the photothermal properties of MnO₂ and the superhydrophobicity of the coating, it could have multiple applications, such as personal thermal management, oil–water separation, and solar-steam generation. This study provides a potential anti-icing/de-icing coating for large-scale preparation and multiple practical applications.

Received 31st August 2023,
 Accepted 19th October 2023

DOI: 10.1039/d3tc03149g

rsc.li/materials-c

1. Introduction

Ice, as a solid form of water, condenses through a freezing environment and is a normal natural phenomenon.^{1–4} However, the accumulation of overlying ice to an excessive volume and mass can have serious consequences. Examples include the: increased weight of transmission lines (which can lead to the collapse of towers);^{5,6} icing of airplane wings (which can lead to flight delays or even disrupt the aerodynamic balance of the flight);^{7,8} icing of wind turbine blades (which can lead to the loss of power generation, resulting in serious economic losses); dislodging of ice (which can result in personal injuries).^{9,10}

Traditional de-icing methods include by mechanical, micro-wave or manual means, which are generally inefficient and

highly energy consuming.^{11–13} Thus, in recent years, passive anti-icing/active de-icing coatings that combine superhydrophobicity with the ability to convert light to heat have shown advantages in terms of energy-saving and environmental protection.^{14–19}

In general, for the fabrication of superhydrophobic surfaces, suitable surface roughness (mainly micro/nano-scale layered structures)^{20–22} and low surface energy are necessary.^{23–26} Usually, in the Wenzel state, droplets are in close contact with the substrate, and the contact area of the solid–liquid interface increases. In the Cassie–Baxter state, the water droplets float on the rough structure and trap an air layer on the solid–liquid surface. The upward aggregation of water droplets reduces the contact area and prevents heat transfer.^{27–29} Methods for preparing rough surfaces include chemical-vapor deposition,^{30,31} chemical etching,^{32,33} and sol–gel methods,^{34,35} or the surface of the substrate can be modified directly with superhydrophobic powders or particles by spraying and immersion methods.^{36,37} Commonly used low-surface-energy substances include fluorosilanes and organosilanes,^{38,39} but fluoride is hazardous to humans and the environment. From the aspect of material selection, MnO₂ has strong light-absorption properties that shows a good photothermal effect, and materials with micrometer size and nanometer size can be prepared by a

^a Key Laboratory of Advanced Structural Materials, Ministry of Education & Advanced Institute of Materials Science, Changchun University of Technology, Changchun 130012, People's Republic of China. E-mail: lw771119@hotmail.com, lixuesong@ccut.edu.cn; Fax: +86-0431-85716426; Tel: +86-0431-85716421

^b School of Science, Changchun Institute of Technology, Changchun, 130012, China

^c State Key Laboratory of Luminescence and Applications, Changchun Institute of Optics, Fine Mechanics and Physics, Chinese Academy of Sciences, Changchun 130033, People's Republic of China

† Electronic supplementary information (ESI) available. See DOI: <https://doi.org/10.1039/d3tc03149g>

simple chemical precipitation method. Microsphere structure and nanoflower structure can increase the surface hydrophobicity by enhancing the microstructural roughness. This micro- and nano- secondary hierarchical structure is the root cause of the superhydrophobicity of the surface.^{40–42} Polydimethylsiloxane (PDMS) has low surface energy, excellent chemical stability, good abrasion resistance and is a fluorine-free polymer binder.^{43–46} Therefore, using them as coating materials can greatly enhance the mechanical stability of the coatings while ensuring an overall hydrophobic situation.

Here, we propose a facile spraying method to prepare superhydrophobic photothermal coatings with surface micro-nano-structures. The coating was a composite of MnO₂ microspheres of diameter ~2.3 μm, MnO₂ nanoflowers of size 300 nm, and PDMS. The coating had excellent superhydrophobicity, with a water contact angle (WCA) of 162.3° and a water sliding angle (WSA) of 2.1°. It also had excellent photothermal-conversion properties and could heat the coating from room temperature to high temperatures (>80 °C) in 300 s under one sun illumination. The coating exhibited excellent anti-icing and de-icing properties, with the ability to prolong icing time and to de-ice rapidly under light-driven conditions. The coating had excellent mechanical durability and maintained good hydrophobicity after extreme tests such as water/sand washing, tape peeling, sonic treatment, UV irradiation, high/low-temperature treatments, sandpaper abrasion, and immersion in acid/alkali solutions. In addition, based on the simple preparation process and good hydrophobicity of the coating, we expanded the coating to oil–water separation, personal thermal management, as well as seawater desalination, wastewater treatment and other aspects of the application, to ascertain its value in photothermal applications.

2. Experimental part

Materials

PDMS and curing agent were purchased from Dow Corning. Ethyl acetate, hydrochloric acid, and sodium hydroxide were purchased from Beijing Chemical Industry Factory. Deionized (DI) water was produced by our research team. Sea sand, sandpaper, cotton fabric, 3 M tapes, acrylic boards, copper plates, aluminum plates, and stainless-steel mesh were all purchased from a local market. Among them, the copper plates and the aluminum plates were polished with sandpaper before use. All experimental drugs were of laboratory grade.

Preparation of materials

Preparation of μm-MnO₂. First, 9.48 g of NH₄HCO₃ was dissolved in 840 ml of DI water and stirred thoroughly to form solution A; 1.81 g of MnSO₄ was dissolved in 840 ml of DI water and 168 ml of ethanol, and stirred thoroughly to form solution B. The two solutions were mixed and stirred for 2 h. The precipitate was collected, washed and dried at 80 °C. Finally, MnO₂ microspheres were formed by heating up to 400 °C in air for 5 h.⁴⁷

Preparation of nm-MnO₂. 0.7 g of KMnO₄ and 1.125 g of MnSO₄ were mixed and added to 440 ml of DI water and stirred at 80 °C for 3 h. After that, the mixture was centrifuged, filtered, washed and dried thoroughly.⁴⁸

Preparation of μm-MnO₂/nm-MnO₂ composite coatings. 0.2 g of μm-MnO₂ and nm-MnO₂ (according to different mass ratios, five groups in total), PMDS precursor and curing agent ratio of 10:1 (total 0.2 g) were mixed. Then, 10 ml of ethyl acetate was used as a solvent to ultrasonicate the materials after mixing and stirring thoroughly. Glass was cleaned and dried. A layer of PDMS coating was sprayed with a spray gun at 45° at a pressure of 2 bar at a distance of 15 cm from the glass, and then cured at 80 °C for 10 min. After that, the composite solution was sprayed and cured at 100 °C for 2 h.

3. Results and discussion

Fig. 1 shows the preparation of anti-icing/de-icing coatings. The coating was formed on glass by spraying using micron-sized and nano-sized MnO₂ (raw material) and PDMS (non-fluorinated polymer binder). In this process, a layer of PDMS was sprayed on the glass substrate first for better thermal insulation and then the composite coating was sprayed.

As shown in Fig. 2a–f, the morphologies of μm-MnO₂, nm-MnO₂ and μm-MnO₂/nm-MnO₂ composite coatings were characterized by scanning electron microscopy (SEM). As shown in Fig. 2a and d, μm-MnO₂ had better dispersion with microspheres of diameter 2.3 μm, along with obvious conical projections on the surface. The SEM images shown in Fig. 2b and e reveal that nm-MnO₂ had a size of ~300 nm with a nanoflower structure consisting of many folded and crossed nanosheets. As can be seen from Fig. 2c and f, nm-MnO₂ was completely covered by PDMS to form clusters, which formed a micro-nano composite structure with μm-MnO₂. The cross-section view in Fig. 2g reveals a porous structure with trapping of a large amount of air which, in turn, achieves superhydrophobic properties by increasing the roughness of the coating surface. Fig. 2h shows the X-ray diffraction (XRD) patterns of μm-MnO₂ and nm-MnO₂. nm-MnO₂ was determined to be α-MnO₂, and μm-MnO₂ was determined to be ε-MnO₂. Fig. 2i shows the UV-Vis-NIR absorption spectra of PDMS coatings and micro-nano-composite coatings. The comparison shows that the composite coating with a surface micro-nano structure had close to 100% light absorption. This excellent light absorption is important for subsequent de-icing and other photothermal-conversion applications.

Fig. 3a shows the variation of WCA by testing different materials on the glass substrate. The pristine bare glass was hydrophilic (WCA = 49.1°). PDMS, as an organosilicon material, has low surface energy and hydrophobic properties. Hence, the hydrophilic surface was transformed into a hydrophobic surface after coating, with a WCA of 104.2°. The hydrophobic property was improved further by adding μm-MnO₂ and nm-MnO₂, respectively. Because of supplying a rougher structure compared with PDMS, the WCA of the micro-coating and

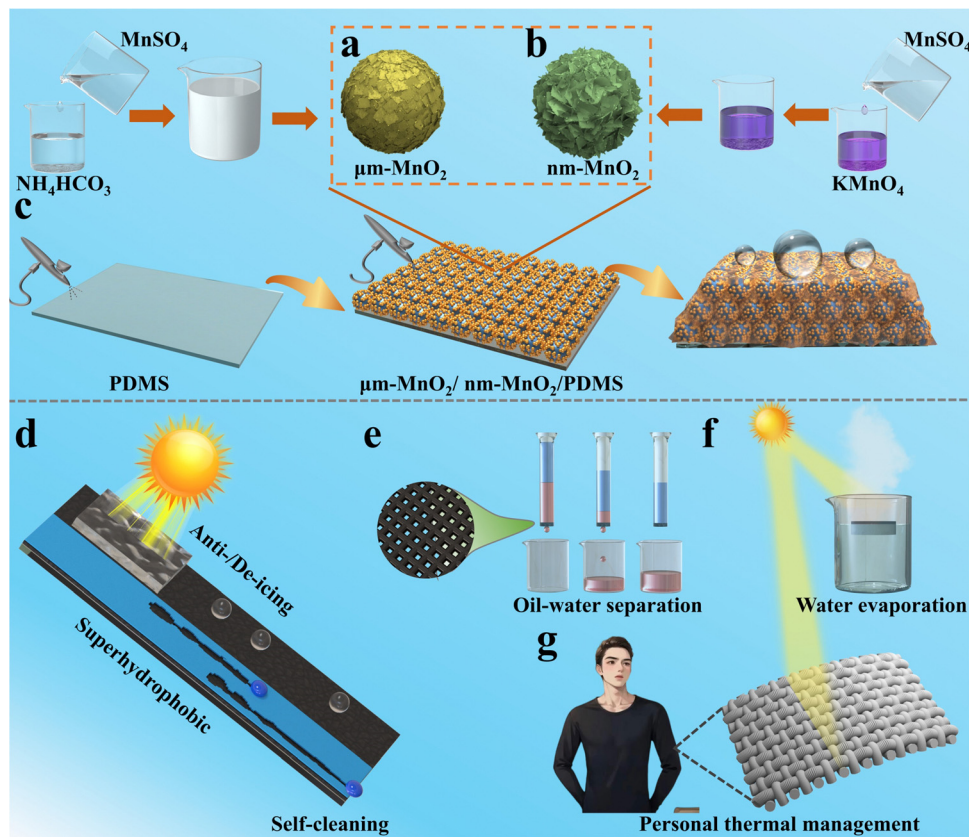


Fig. 1 Preparation of a superhydrophobic photothermal coating (schematic).

nano-coating became 154.8° and 137.1° , respectively. The composite coating with micro- and nano-structures had the best hydrophobicity, with a WCA of 162.3° , due to two key factors: high roughness and low surface energy. In addition, different liquids (water, milk, methylene blue solution and tea) were dropped upon the coatings to observe their hydrophobicity (Fig. S1, ESI[†]). The different types of liquids were in the form of round beads on the coatings and, thus, showed good superhydrophobicity. In order to test the hydrophobicity of the coating sprayed on different kinds of substrates, four substrate materials (glass, acrylic board, polished copper plate, and polished aluminum plate) were selected, and the WCA was measured by adding drops of water on the surface (Fig. S2, ESI[†]). The WCAs of the coatings on different substrates were all over 160° , which revealed superhydrophobicity. Fig. S3 (ESI[†]) summarizes the WCAs of the different kinds of materials on the glass substrate, the different kinds of substrates, and the different mass ratios of MnO_2 . The composite coatings with micro-nano structures exhibited superhydrophobicity. The voids and roughness of the micro- and nanostructures could be “tuned” by adjusting the different ratios of $\mu\text{m-MnO}_2$ and nm-MnO_2 . Fig. S4 (ESI[†]) shows the SEM and atomic force microscopy (AFM) images of microspheres and nanoflowers with different ratios. Among them, when the ratio was 4 : 6, the coating presented the roughest surface (consistent with SEM and WCA results), and the rougher surface led to more air

layers between droplets and the coating surface, which was the main reason for the best hydrophobicity at this ratio.

As shown in Fig. 3b and Movie S1 (ESI[†]), a typical “silver mirror” phenomenon was observed when the composite coating was immersed in water.^{49,50} This was due to the air layer on the surface of the coating being captured by the superhydrophobic surface. As shown in Fig. 3c (Movie S2, ESI[†]), when a water jet was sprayed onto the coating, it bounced directly on the surface to form an angle. After being washed under the faucet on the coating surface, no water droplets remained, indicating its good superhydrophobicity. In Fig. S5 (ESI[†]), the droplets hovering on the syringe could not adhere to the surface of the superhydrophobic coating even after squeezing or stretching, which demonstrated the low adhesion between the droplets and coating. As shown in Fig. 3d (Movie S3, ESI[†]), by continuously adding water droplets to the coating using a dropper after adjusting the angle of the tilted platform to 3° , small droplets quickly slipped off the coating and gathered underneath the platform, proving its good hydrophobicity under a small angle of tilt. Self-cleaning is one of the important properties of superhydrophobic surfaces.^{51–53} In Fig. 3e (Movie S4, ESI[†]), CuSO_4 was covered on the coating at a certain inclination angle. When the water droplets rolled down quickly, the CuSO_4 on the trajectory of the water droplets was removed effectively, and satisfactory self-cleaning properties were demonstrated. To better show this self-cleaning effect, we used

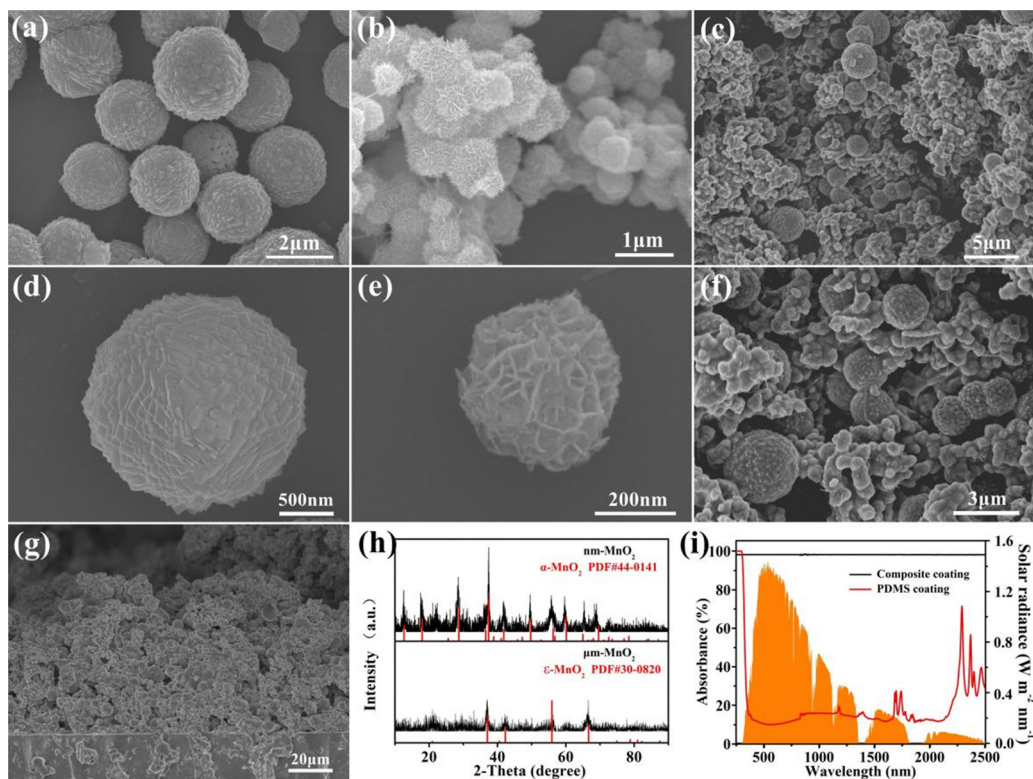


Fig. 2 (a)–(c) Low-magnification SEM images of $\mu\text{m-MnO}_2$, nm-MnO₂, and composite coatings. (d)–(f) High-magnification SEM images of $\mu\text{m-MnO}_2$, nm-MnO₂, and composite coatings. (g) Cross-sectional SEM image of the composite coating. (h) XRD analysis of $\mu\text{m-MnO}_2$ and nm-MnO₂. (i) UV-Vis-NIR absorption spectra of PDMS coatings and composite coatings.

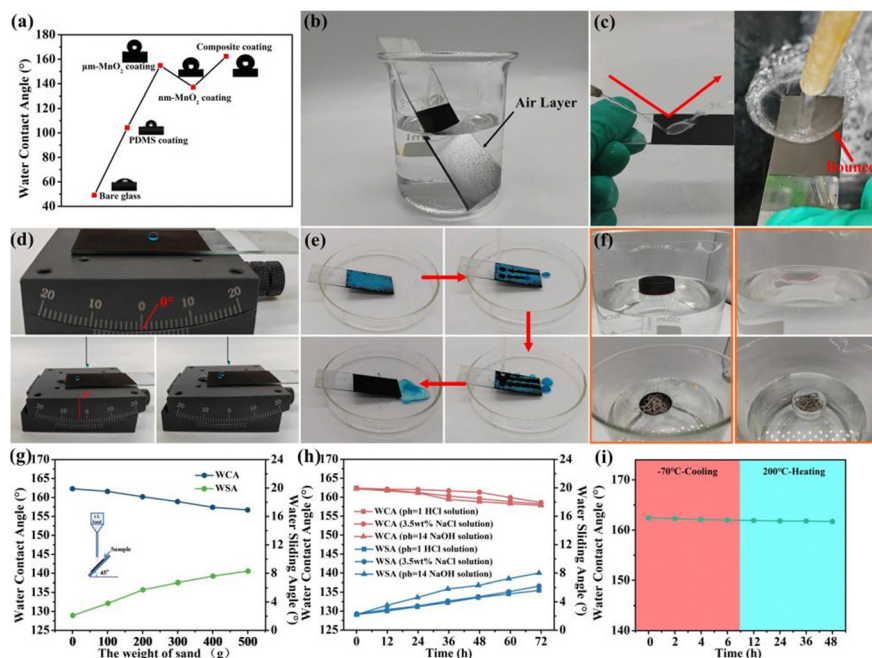


Fig. 3 (a) WCA of different materials on a glass substrate. (b) "Silver mirror"-like phenomenon of superhydrophobic photothermal coatings. (c) Water column and water flow washing over the coating surface. (d) Water droplets flowing down from the small-angle platform. (e) CuSO₄ particles simulating self-cleaning phenomena. (f) Coated/uncoated Petri dishes placed on a water surface. (g) Resistance to the gravel-impact test. (h) Resistance to corrosion by acid, alkali and salt solution. (i) High- and low-temperature test.

methylene-blue dye to simulate small-sized dust in air, and the results are shown in Fig. S6 (ESI†). If an object is placed on the water surface, the surface tension of the water forms a pressure difference between the object and water. This pressure difference can offset the gravity of the object, which makes the object float on the water surface, giving it a certain carrying capacity. In the present study, Petri dishes with or without sprayed composite coatings were used to investigate the improvement of the superhydrophobic coating on the carrying capacity of the objects. In Fig. 3f, the superhydrophobic coated Petri dish floats on the water surface as a whole in the unloaded state, whereas the bare Petri dish is mostly in the water. In the subsequent maximum loading-capacity tests (Fig. S7 and S8, ESI†), the bare Petri dish (self-weight 8 g) sank into the water after placing an object of 8 g (16 crank pins), whereas the Petri dish with a hydrophobic coating sank into the water after placement of an object of 12 g (24 crank pins), and the overall loading capacity was improved.

Mechanical properties are also important. In particular, functional coatings inevitably work in complex environments, such as small-particle erosion or rainfall impact, in practical applications.^{54–56} Therefore, a series of tests (resistance to sandstone impact, water-current impact, corrosion by acid, alkali and salt solution, sandpaper abrasion, and high/low temperature variations) were undertaken (Fig. 3g–i and Fig. S9, ESI†). As shown in Fig. 3g, 100 g of quartz sand (300 mesh) at a time was released in free fall from a height of 45 cm onto a 45°-inclined coated surface. The sand slid along the surface, and the WCA and WSA of the coating surface were tested after each complete release. The WCA of the coating became smaller and the WSA became larger after the cyclic impact of sand particles due to the slight abrasion of the microstructure of the coating surface caused by the impact of sand particles. Fig. 3h and i show the WCAs in different solutions and temperatures. The surface properties of the coatings were intact and hydrophobicity was not significantly reduced after 72 h immersion in different solutions and 48 h placement under extreme temperature conditions. The PDMS in the composite coating, due to its chemical inertness, could provide a chemical barrier for the entire coating, protect the coating and the substrate under the coating from corrosion by acids and alkalis, and provide long-lasting hydrophobicity (Fig. S10, ESI†). A comparative observation by SEM before and after sandpaper abrasion (Fig. S11, ESI†) showed many large voids and air layers in the coating before abrasion whereas, after abrasion, the pores between the clusters and particles gradually became smaller, and the whole structure tended to be more compact and dense. As the number of sandpaper abrasions increased, the most superficial particles at the top of the coating were rubbed off, while the interior of the coating maintained its micro- and nanostructure and continued to provide superhydrophobicity. It is not until the particles in the coating are almost completely worn away by the sandpaper that a serious degradation in superhydrophobicity is likely to occur. The coating had excellent resistance to abrasion, but it also had great adhesion strength to the substrate

(Fig. S12, ESI†). Using a razor blade, a pattern of intersecting grids was etched into the coating. Subsequently, these grids adhered to 3 M tape, which was peeled off quickly after repeated pressing with a 200 g weight. No obvious coating blocks were observed to fall off after removing the 3 M tape, and the adhesion level of the coating could be categorized as level I according to the standard GB/T9286.^{57,58} After several episodes of tape-stripping, the water droplets still good hydrophobic properties on the coating surface. However, on the platform with a small angle tilt (Fig. S13, ESI†), the water droplets rolled down quickly without residue, which suggested good adhesion between the coating and substrate, and good hydrophobic properties. Meanwhile, we tested the bond strength between PDMS and glass using a tensile machine (Fig. S14, ESI†). The bond strength between PDMS and glass could reach 528 N, which also indicated that the adhesion between the two was relatively good. The impact resistance of the coatings was tested (Fig. S15, ESI†) when 20 g steel balls were repeatedly dropped from a height of 100 cm. Although the aluminum plate underwent bending deformation, the surface of the coatings did not peel off or become damaged, and the superhydrophobicity was unchanged.

The photothermal properties of composite coatings were investigated. Fig. 4a, d–f, and Fig. S16 (ESI†) show the curves and infrared photographs of the temperature change with time under different light intensities. With increasing light intensity, the surface temperature of the coating increased, and the temperature of the layer reached equilibrium within 300 s for different light intensities. The temperature decreased rapidly and returned to room temperature after removal of the light source. Cycling the composite coatings through light and cooling led to highly similar photothermal responses and maximum equilibrium temperatures over the five cycles tested (Fig. 4b), which demonstrated the stability of the coatings under photothermal conditions. As seen from Fig. S17 (ESI†), the equilibrium temperature (T) at different light intensities showed a closely corresponding linear relationship with light intensity (L). We also explored the temperature change when the coating surface was shaded taking sand as an example. In Fig. 4c, the maximum equilibrium temperature can reach 82 °C when the surface is not shaded; when the surface is covered by sand, the temperature drops to 52.5 °C. Due to the good self-cleaning effect, the coating will be cleaned up if water flows over the sand, while the photothermal temperature returns to normal (Fig. S18, ESI†). Hence, good self-cleaning performance had an important role for photothermal coatings. The equilibrium temperature of the coating returned to the initial temperature after the surface had been cleaned, so good self-cleaning ensured the long-lasting stability of the coating in photothermal applications.

Freezing from water to ice goes through three processes.^{59,60} When the temperature of the droplet begins to fall to 0 °C, this is called the “supercooling” stage. When the water begins to change from the liquid state to solid ice, the entire droplet presents a mixture of ice and water, and this is known as the “phase change” stage. When the droplet is completely freezing

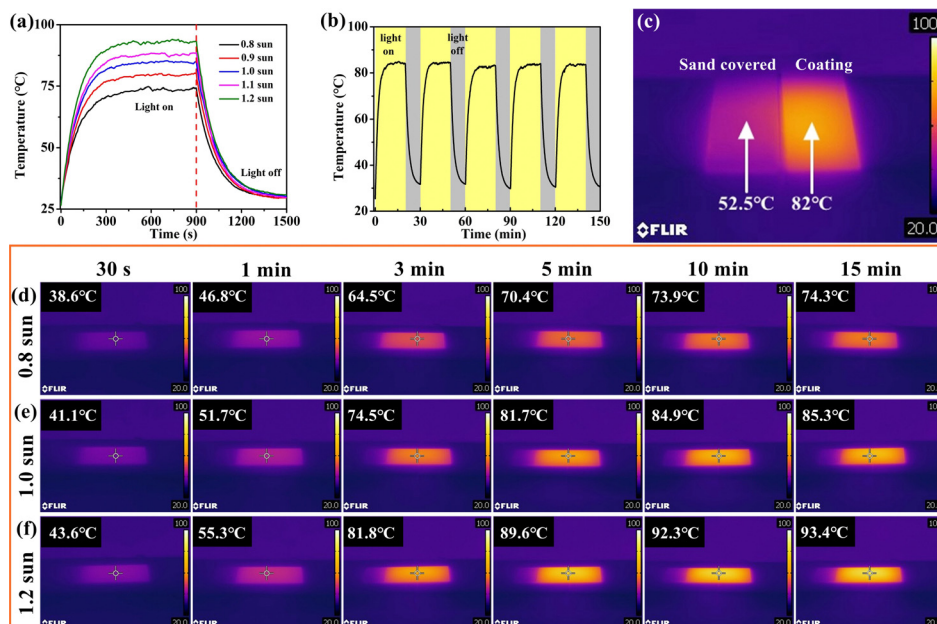


Fig. 4 (a) Temperature-variation curves of composite coatings at different light intensities. (b) Photothermal conversion of composite coatings in five heating-cooling cycles. (c) Self-cleaning and infrared temperature images of the composite coating at 1 sun intensity. (d)–(f) Infrared temperature images of the coating at different light intensities.

from the liquid water into a solid state of ice, this is known as the “completely freezing” stage. The time of freezing of the whole droplet can be considered to be the time required from the beginning of the droplet reaching 0 °C to complete freezing into ice. From Fig. 5a, b and Fig. S19 (ESI[†]), one can see the

beginning of the ice–water mixing state, the temperature change of releasing the latent heat, the state of ice droplets after complete freezing, and the time taken. When on the bare glass surface, due to the hydrophilicity, the water droplets spread out quickly and form a small “ice mound” after

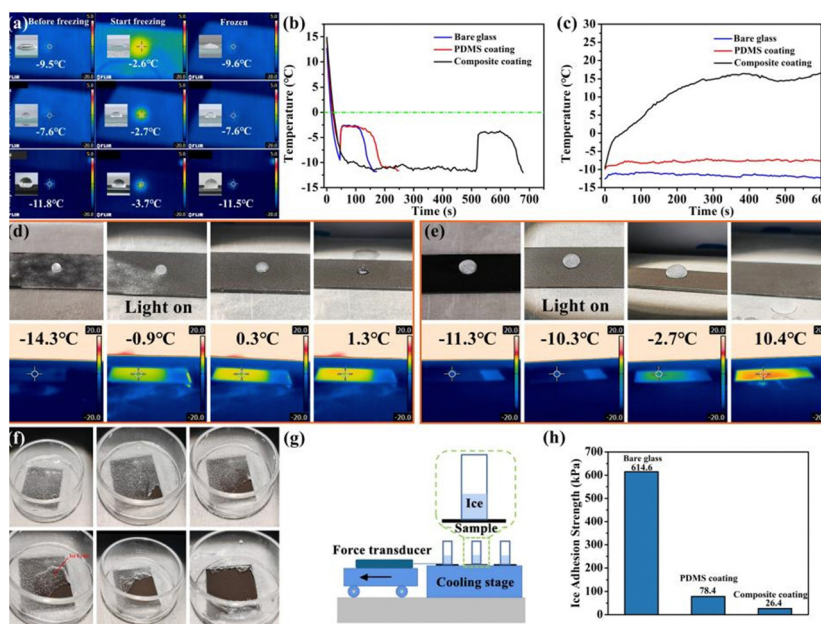


Fig. 5 (a) Infrared images of water droplets during freezing and the corresponding temperatures; the inset shows the corresponding water morphology. (b) Freezing time–temperature curves for three coatings in a –15 °C environment. (c) Temperature-change curves of three coatings in a –15 °C environment and with 1 sun intensity added. (d) Ice melting of a 30 µl water droplet in light. (e) Ice melting of a 300 µl water droplet in light. (f) De-icing of an ice layer on the coating with a thickness of ~2 mm during light illumination. (g) Ice-adhesion test (schematic). (h) Ice-adhesion strength of different coatings.

complete freezing with a freezing time of 127 s. The PDMS coating, due to its hydrophobicity, leads to ice droplets forming a hemispherical shape after freezing, and simultaneously the freezing time (152 s) is increased slightly. The composite coating, due to its superhydrophobicity, remains spherical after freezing and effectively extends the freezing time to 655 s. In order to further investigate the effect of a highly humid environment on delayed icing, we undertook a control experiment at 80% humidity. As shown in Fig. S20 (ESI[†]), the time of delayed icing was shortened to 515 s under high humidity conditions and, simultaneously, the coating surface became frosted with a lot of ice. Thus, it was easier to form ice under high humidity conditions than low humidity conditions. Fig. 5c shows the temperature change of the coating surface after illumination by 1 sun intensity in a $-15\text{ }^{\circ}\text{C}$ environment. For the bare glass and PDMS coating, the temperature after exposure to light did not change greatly. The composite coating, due to the addition of MnO_2 , the temperature after being exposed to light increased and stabilized at $16\text{ }^{\circ}\text{C}$, which prevented icing occurring. Even if the superhydrophobicity of the coating exhibited excellent anti-icing properties, ice could form on the surface of the coating after prolonged exposure at lower temperatures. Therefore, it is important to develop multifunctional surfaces that combine passive anti-icing and active de-icing. To investigate the photothermal de-icing performance under actual freezing weather, the de-icing performance of the composite coatings was tested under 1 sun intensity, and the temperature change of droplets was monitored at an ambient temperature of $-15\text{ }^{\circ}\text{C}$ and relative humidity of $35 \pm 5\%$. When $30\text{ }\mu\text{l}$ and $300\text{ }\mu\text{l}$ of water droplets were placed, respectively, on the coating (as shown in Fig. 5d and e), the ice droplets remained beaded in the frozen state due to the good superhydrophobicity of the composite coating. The infrared-temperature image revealed that the coating surface temperature started to rise after light irradiation. The ice droplets started to melt into a mixed state of ice and water. The small ice droplets melted completely after 42 s, and large ice droplets melted and rolled off from the coating surface after 186 s. The effects of the angle of inclination on the melting time were compared (Fig. S21 and Fig. 5e, ESI[†]). At the horizontal angle, the ice on the coating surface needed to melt completely. At a tilt angle, when the ice started to be in the ice–water state, the ice droplets could be dislodged directly from the coating surface. This action reduced the melting time while avoiding refreezing in cold conditions. Simulated ice accumulation was used to freeze out a 2 mm-thick ice layer on the coating. The sample was placed on a cooling table at $-15\text{ }^{\circ}\text{C}$ while 1 sun intensity of light was applied. The outdoor light intensity can be affected by weather and other factors, so we simulated the de-icing performance at a lower solar intensity (0.8 sun), as shown in Fig. S22 (ESI[†]). At low light intensity, although the temperature of the coating surface also increased, the rate of temperature increase was significantly slower, while the time to melt $30\text{ }\mu\text{l}$ droplets was 76 s, which was delayed by 34 s compared with that using 1 sun light intensity (42 s). Fig. 5f shows the de-icing process of the ice layer. The ice layer

gradually melted from the inside, and bubbles appeared at the coating–ice junction, which helped to reduce the adhesion between the ice layer and the coating. Simultaneously, with continuous irradiation by the light source, the ice shell melted first inside the ice layer, and this phenomenon indicated that the coating converted the light into heat energy and carried out effective heat transfer. After 254 s, the ice layer on the coating melted completely, and no water droplets remained on the coating surface. Furthermore, a self-made device was used to test the adhesion strength of ice, as shown in Fig. 5g. First, an ice column was frozen on the sample and placed on a cooling table. Then, the force sensor was fixed on the rail sliding table driven by a servomotor, and the ice column was pulled at a certain speed at a constant rate. When the ice column was completely detached from the interface of the coating, the transient maximum pulling force was recorded and the ice adhesion strength was calculated as shown in Fig. 5h. The ice adhesion strength of the bare glass surface was 614.6 kPa, and that of the PDMS coating with low surface energy decreased to 78.4 kPa. The ice adhesion strength of the composite coating decreased to 26.4 kPa. It has been shown that if the ice adhesion strength is $<50\text{ kPa}$, then ice accumulation can be removed by natural wind or vibration.

The composite coating could be attached to different substrates by simple spraying. Hence, it could also be sprayed on fabrics to prepare large-sized superhydrophobic photothermal materials ($50\text{ cm} \times 50\text{ cm}$) (Fig. 6a). Commercially available cotton fabrics are usually hydrophilic. The composite coated fabric maintained good hydrophobicity (Fig. 6b), and water droplets quickly slid off without any residue after contacting the coating, maintaining a good self-cleaning performance (Fig. S23, ESI[†]). Simultaneously, the coated fabric maintained good air permeability (Fig. 6c), where a piece of coated fabric covered a bottle mouth containing ammonia and hydrochloric acid. Due to the volatile nature of hydrochloric acid, it reacts with ammonia to form ammonium chloride, so white smoke would be seen above the fabric. Fig. 6d–f, and Fig. S24 (ESI[†]) show a comparison of the temperature change of a commercial white fabric, a commercial black fabric, and a composite coated fabric at 1 sun intensity. The compound-coated fabric heated up faster and had a higher final equilibrium temperature at 1 sun intensity, which was $51\text{ }^{\circ}\text{C}$ higher than the commercially available white fabric ($41.9\text{ }^{\circ}\text{C}$) and $4\text{ }^{\circ}\text{C}$ higher than the commercially available black fabric ($89\text{ }^{\circ}\text{C}$). Composite-coated fabrics can be used effectively in applications based on personal thermal management due to their higher equilibrium temperatures, which provides better heating capacity for the human body in cold environments.

After spraying the composite coating on stainless-steel mesh, the mesh was uniformly encapsulated by the coating and exhibited superhydrophobicity (Fig. S25, ESI[†]). When an oily solution was placed on the stencil mesh, it penetrated quickly and the oil contact angle revealed that it was superoleophilic (Fig. 6g and Fig. S26, ESI[†]). Therefore, it could also be used for oil–water separation. This separation process is shown in Fig. 6h, where a mixture containing 30 ml of *n*-hexane

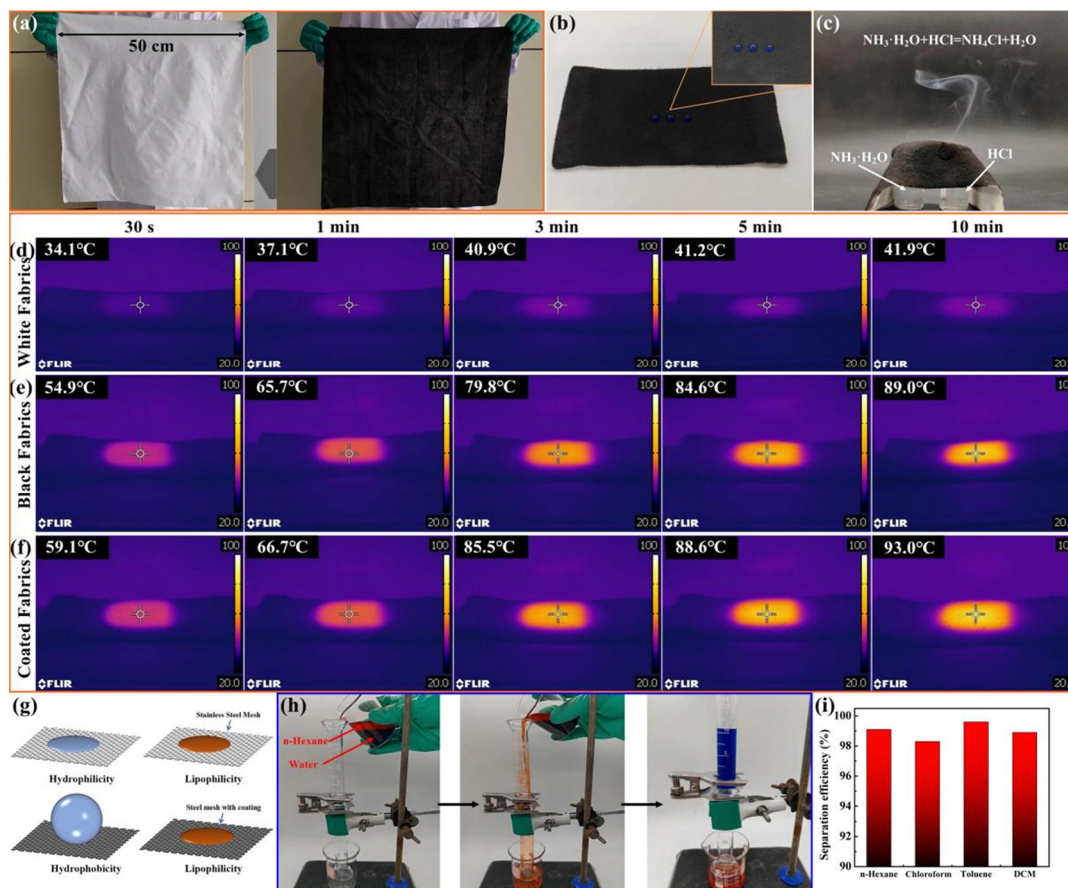


Fig. 6 (a) Original and coated fabrics. (b) Detail of the hydrophobic coated fabric. (c) Breathability of the hydrophobic coated fabric. (d)–(f) Temperature change of commercial white fabric, commercial black fabric, and hydrophobic coated fabric at 1 sun intensity. (g) Oleophilic hydrophobicity of stainless-steel mesh (schematic). (h) Oil–water separation. (i) Efficiency of oil–water separation.

(Oil Red O staining) and 20 ml of water (methylene-blue staining) was mixed, and a sprayed composite-coated stencil was placed in the middle of two measuring cups. After pouring the liquid slowly, *n*-hexane could penetrate into the beaker quickly due to its lipophilicity, while the water was intercepted above the stainless-steel mesh. Fig. 6i shows the separation efficiency of applying hydrophobic and lipophilic properties to several other oily liquids, such as chloroform, toluene, and DCM. The prepared stainless-steel mesh achieved a separation efficiency > 98% for the mixed liquids.

In recent years, the application of photothermal conversion has been widely used for generation of interfacial solar vapor.^{61–64} Composite coating material was sprayed on the surface of melamine sponge to prepare a Janus solar evaporator with hydrophobic/hydrophilic properties. A sponge is a hydrophilic material that cannot float on a water surface by itself after fully absorbing water. The prepared composite coating could give the sponge hydrophobic properties. From Fig. 7a and Fig. S27 (ESI[†]), it can be seen that the surface of the pristine sponge was smooth, while the structure of the sprayed sponge was completely encapsulated by the coating and, thus, showed good hydrophobicity. Due to the good photothermal properties of the coating and the unique porous structure of the sponge, it showed high equilibrium temperatures under different light

intensities in dry environments (Fig. 7b and Fig. S28, ESI[†]) and in water (Fig. 7c and Fig. S29, ESI[†]), and equilibrium temperature was > 100 °C in dry environments at 1.2 sun intensity. Fig. 7d shows that the evaporation rate of pure water under 1 sun intensity was only 0.45 kg m⁻² h⁻¹, while that of the coated sponge could reach 1.7 kg m⁻² h⁻¹, which was 3.7 times faster than that of pure water, and the efficiency of photothermal conversion reached 92.6%. The rate of water evaporation was attributed to the good photothermal properties of the upper hydrophobic surface. If water is transported to a high-temperature surface, it is heated and converted into steam, and the water vapor diffuses into the air through the open pores. The sponge has its own insulating properties and the uncoated portion of the sponge was hydrophilic for continuous transport of moisture. Fig. 7e shows the purification effect on microbial bacteria before and after water evaporation. The water contained a large number of microbial colonies before purification, while the purified water was almost free of bacterial colonies. Fig. 7f and Fig. S30 (ESI[†]) show the purification effect of the coated sponge for dyes. The characteristic peaks of methyl orange, rhodamine B and methylene blue disappeared after purification. According to optical photographs, the purified water was transparent. The pH of acid and alkali solutions before and after evaporation is shown in Fig. 7g, and the pH of

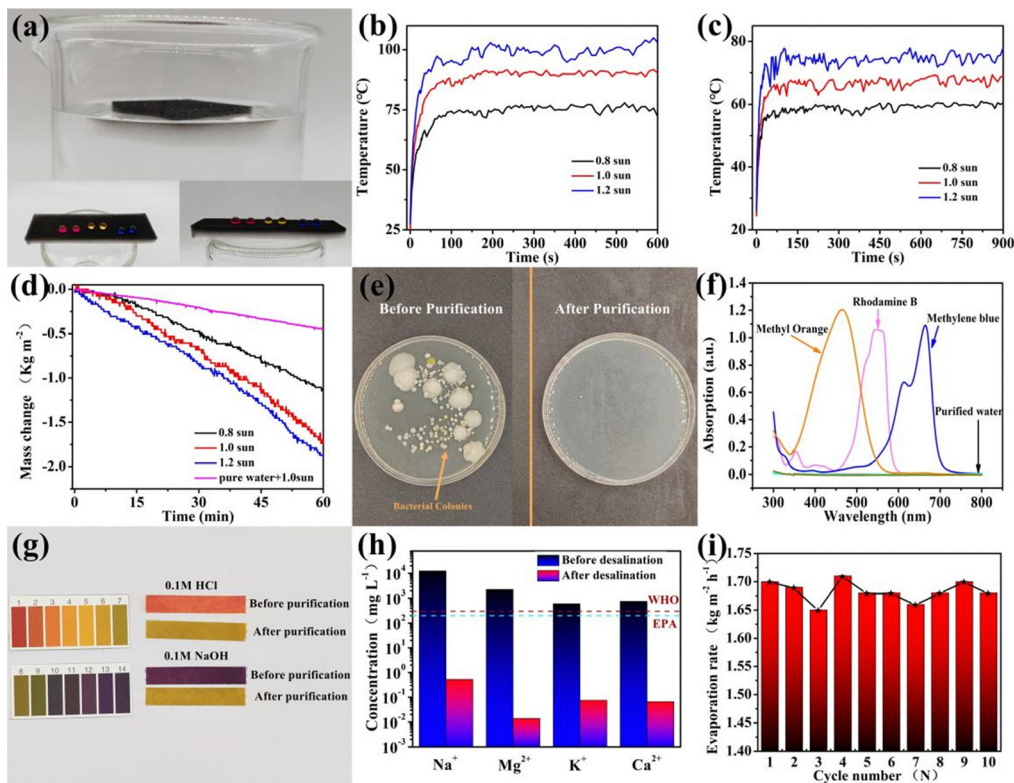


Fig. 7 (a) Janus sponge in water. (b) Temperature changes of the sponge in a dry environment (air) at different light intensities. (c) Temperature changes of sponges in a wet environment (water) at different light intensities. (d) Evaporation rates of sponges at different light intensities. (e) Microbial bacteria in water before and after evaporation. (f) Purification of dyes before and after evaporation. (g) pH of acid and alkali solutions before and after evaporation. (h) Metal-ion concentration before and after evaporation. (i) Ten cycles of the evaporation rate.

the purified water was found to be 7. Fig. 7h shows the rejection rate of the coated sponge for heavy-metal ions (Na^+ , Mg^{2+} , K^+ , Ca^{2+}) in wastewater. The ionic concentration in purified water was reduced by 2–3 orders of magnitude, and the quality of the purified water was also in full compliance with World Health Organization and US Environmental Protection Agency standards for potable water.^{65,66} The cyclic stability of the evaporation of the coated sponge was tested (Fig. 7i) 10 times for 1 h each time. The cyclic stability remained $>1.65 \text{ kg m}^{-2} \text{ h}^{-1}$, which suggested that the coated sponge had good continuous cyclic stability.

4. Conclusions

A two-size MnO_2/PDMS superhydrophobic coating with a surface micro-nano structure was demonstrated in this work. The coating had good self-cleaning, effective anti-icing and sunlight-responsive de-icing properties due to its low surface energy and photothermal-conversion properties. The micro-nano two-size MnO_2/PDMS superhydrophobic coating trapped the air layer under the water droplets efficiently. Simultaneously, it could withstand a variety of mechanical-durability tests, including impact with 500 g of sand gravel, 100 times of tape peeling, 72 h of immersion in strong acid/strong alkali solutions, and razor-blade scraping. Based on such excellent performance, the coating could be sprayed on: cotton fabrics

for personal heat management; stainless-steel mesh for efficient oil–water separation; a sponge to form the Janus solar evaporator. The coating had an evaporation rate of $1.7 \text{ kg m}^{-2} \text{ h}^{-1}$ under 1 sun intensity, and could be suitable for practical applications in solar desalination. Therefore, this work provides a feasible strategy for the development of solar-powered multifunctional superhydrophobic coatings.

Conflicts of interest

There are no conflicts to declare.

Acknowledgements

This research was supported by grants from the National Natural Science Foundation of China (62004015 and 62004014), Department of Science and technology of Jilin Province (20210101077JC), and the Natural Science Foundation of Jilin Province (20200201381JC).

References

- P. Irajizad, A. Al-Bayati, B. Eslami, T. Shafquat, M. Nazari, P. Jafari, V. Kashyap, A. Masoudi, D. Araya and H. Ghasemi, *Mater. Horiz.*, 2019, **6**, 758–766.

- 2 K. Golovin, A. Dhyani, M. D. Thouless and A. Tuteja, *Science*, 2019, **364**, 371–375.
- 3 Y. Shen, X. Wu, J. Tao, C. Zhu, Y. Lai and Z. Chen, *Prog. Mater. Sci.*, 2019, **103**, 509–557.
- 4 J. F. Wei, B. C. Li, N. Tian, J. J. Zhang, W. D. Liang and J. P. Zhang, *Adv. Funct. Mater.*, 2022, **32**, 2206014.
- 5 X. Wei, Z. Jia, Z. Sun, Z. Guan and M. Farzaneh, *IEEE Trans. Dielectr. Electr. Insul.*, 2015, **22**, 400–408.
- 6 Q. Li and Z. Guo, *J. Mater. Chem. A*, 2018, **6**, 13549–13581.
- 7 S. K. Thomas, R. P. Cassoni and C. D. MacArthur, *J. Air.*, 1996, **33**, 841–854.
- 8 O. Parent and A. Ilinca, *Cold. Reg. Sci. Technol.*, 2011, **65**, 88–96.
- 9 S. Zhang, J. Huang, Y. Cheng, H. Yang, Z. Chen and Y. Lai, *Small*, 2017, **13**, 1701867.
- 10 T. Zhu, Y. Cheng, J. Huang, J. Xiong, M. Ge, J. Mao, Z. Liu, X. Dong, Z. Chen and Y. Lai, *Chem. Eng. J.*, 2020, **399**, 125746.
- 11 L. Pan, Z. Liu, O. Kızıltaş, L. Zhong, X. Pang, F. Wang, Y. Zhu, W. Ma and Y. Lv, *Compos. Sci. Technol.*, 2020, **192**, 108117.
- 12 L. Ding, X. Wang, W. Zhang, S. Wang, J. Zhao and Y. Li, *Appl. Sci.*, 2018, **8**, 2360.
- 13 S. Luo and X. Yang, *Constr. Build. Mater.*, 2015, **94**, 494–501.
- 14 L. Zhang, B. C. Luo, K. Fu, C. L. Gao, X. F. Han, M. L. Zhou, T. C. Zhang, L. S. Zhong, Y. P. Hou and Y. M. Zheng, *Adv. Sci.*, 2023, 202304187.
- 15 W. Zheng, L. Teng, Y. Lai, T. Zhu, S. Li, X. Wu, W. Cai, Z. Chen and J. Huang, *Chem. Eng. J.*, 2022, **427**, 130922.
- 16 H. Xie, W. H. Xu, Y. Du, J. Gong, R. Niu, T. Wu and J. P. Qu, *Small*, 2022, **18**, 2200175.
- 17 H. Guo, M. Liu, C. Xie, Y. Zhu, X. Sui, C. Wen, Q. Li, W. Zhao, J. Yang and L. Zhang, *Chem. Eng. J.*, 2020, **402**, 126161.
- 18 Y. Li, W. Ma, Y. S. Kwon, W. Li, S. Yao and B. Huang, *Adv. Funct. Mater.*, 2022, **32**, 2113297.
- 19 Y. Liu, R. Sun, B. Jin, T. Li, L. Yao, L. Feng and J. He, *ACS Appl. Nano Mater.*, 2022, **5**, 5599–5608.
- 20 W. Barthlott and C. Neinhuis, *Planta*, 1997, **202**, 1–8.
- 21 L. Feng, S. Li, Y. Li, H. Li, L. Zhang, J. Zhai, Y. Song, B. Liu, L. Jiang and D. Zhu, *Adv. Mater.*, 2002, **14**, 1857–1860.
- 22 R. Zhang, J. F. Wei, N. Tian, W. D. Liang and J. P. Zhang, *ACS Appl. Mater. Interfaces*, 2022, **14**, 49047–49058.
- 23 H. Xie, J. F. Wei, S. Y. Duan, Q. Zhu, Y. F. Yang, K. Chen, J. J. Zhang, L. X. Li and J. P. Zhang, *Chem. Eng. J.*, 2022, **428**, 132585.
- 24 G. Han, T. B. Nguyen, S. Park, Y. Jung, J. Lee and H. Lim, *ACS Nano*, 2020, **14**, 10198–10209.
- 25 Y. Zhuo, V. Hakonsen, Z. He, S. Xiao, J. He and Z. Zhang, *ACS Appl. Mater. Interfaces*, 2018, **10**, 11972–11978.
- 26 Y. Qing, C. Yang, N. Yu, Y. Shang, Y. Sun, L. Wang and C. Liu, *Chem. Eng. J.*, 2016, **290**, 37–44.
- 27 W. G. Bae, H. N. Kim, D. Kim, S. H. Park, H. E. Jeong and K. Y. Suh, *Adv. Mater.*, 2014, **26**, 675–700.
- 28 T. L. Liu and C. J. Kim, *Science*, 2014, **346**, 1096–1100.
- 29 T. S. Wong, S. H. Kang, S. K. Tang, E. J. Smythe, B. D. Hatton, A. Grinthal and J. Aizenberg, *Nature*, 2011, **477**, 443–447.
- 30 H. Tavana, A. Amirfazli and A. W. Neumann, *Langmuir*, 2006, **22**, 5556–5559.
- 31 J. Yu, L. Qin, Y. Hao, S. Kuang, X. Bai, Y. M. Chong, W. Zhang and E. Wang, *ACS Nano*, 2010, **4**, 414–447.
- 32 L. Liu, F. Xu and L. Ma, *J. Phys. Chem. C*, 2012, **116**, 18722–18727.
- 33 E. Vazirinasab, R. Jafari and G. Momen, *Surf. Coat. Technol.*, 2018, **341**, 40–56.
- 34 M. Ramezani, M. R. Vaezi and A. Kazemzadeh, *Appl. Surf. Sci.*, 2014, **317**, 147–153.
- 35 M. Poddighe and P. Innocenzi, *Materials*, 2021, **14**, 6799.
- 36 C. Wu, Q. Liu, R. Chen, J. Liu, H. Zhang, R. Li, K. Takahashi, P. Liu and J. Wang, *ACS Appl. Mater. Interfaces*, 2017, **9**, 11106–11115.
- 37 V. S. Saji, *J. Magn. Alloys*, 2021, **9**, 748–778.
- 38 H. Chen, F. Wang, H. Fan, R. Hong and W. Li, *Chem. Eng. J.*, 2021, **408**, 127343.
- 39 G. Jiang, Z. Liu and J. Hu, *Adv. Mater. Interfaces*, 2021, **9**, 2101704.
- 40 W. Zeng, H. Zhang, Y. Deng, A. Jiang, X. Bao, M. Guo, Z. Li, M. Wu, X. Ji, X. Zeng and L. Mei, *Chem. Eng. J.*, 2020, **389**, 124494.
- 41 B. Ma, Y. Nishina and A. Bianco, *Carbon*, 2021, **178**, 783–791.
- 42 S. Dawadi, A. Gupta, M. Khatri, B. Budhathoki, G. Lamichhane and N. Parajuli, *Bull. Mater. Sci.*, 2020, **43**, 277.
- 43 M. Ge, C. Cao, F. Liang, R. Liu, Y. Zhang, W. Zhang, T. Zhu, B. Yi, Y. Tang and Y. Lai, *Nanoscale Horiz.*, 2020, **5**, 65–73.
- 44 S. Barthwal and S.-H. Lim, *J. Membr. Sci.*, 2021, **618**, 118716.
- 45 T. X. Zhu, Y. M. Ni, K. Y. Zhao, J. Y. Huang, Y. Cheng, M. Z. Ge, C. Park and Y. K. Lai, *ACS Nano*, 2022, **16**, 18018–18026.
- 46 T. X. Zhu, L. X. Liu, J. Y. Huang, S. H. Li, Y. G. Lei, W. L. Cai, Y. K. Lai and H. Q. Li, *J. Mater. Sci. Technol.*, 2023, **138**, 108–116.
- 47 C. Liu, X. Zhang, H. Shang, S. Li, Z. Wen, S. Ji and J. Sun, *J. Alloys Compd.*, 2021, **876**, 160113.
- 48 S.-L. Chiam, S.-Y. Pung, F. Y. Yeoh and M. Ahmadipour, *Mater. Chem. Phys.*, 2022, **280**, 125848.
- 49 L. Zhang, C. Gao, L. Zhong, L. Zhu, H. Chen, Y. Hou and Y. Zheng, *Chem. Eng. J.*, 2022, **446**, 137461.
- 50 H. He, W. Huang and Z. Guo, *Mater. Today Phys.*, 2023, **30**, 100927.
- 51 K. Li, J. Xiang, J. Zhou, X. Su, H. Xie, S. Lin, Z. Xiao, W. Huang, C. Zhao, H. Chen and W. Wu, *Prog. Org. Coat.*, 2023, **177**, 107415.
- 52 T. Wu, W.-H. Xu, K. Guo, H. Xie and J.-P. Qu, *Chem. Eng. J.*, 2021, **407**, 127100.
- 53 W. Li, K. Liu, Y. Zhang, S. Guo, Z. Li and S. C. Tan, *Chem. Eng. J.*, 2022, **446**, 137195.
- 54 Z. Zhao, H. Chen, Y. Zhu, X. Liu, Z. Wang and J. Chen, *Compos. Sci. Technol.*, 2022, **227**, 109578.

- 55 C. Su, L. Zhou, C. Yuan, X. Wang, Q. Zhao, X. Zhao and G. Ju, *Compos. Sci. Technol.*, 2023, **231**, 109785.
- 56 H. Xie, Y. Du, W. Zhou, W. Xu, C. Zhang, R. Niu, T. Wu and J. Qu, *Small*, 2023, **19**, 2300915.
- 57 L. Jiang, M. Han, J. Sun, M. Gong, Y. Lin, T. Xiao, P. Xiang, W. Chen and X. Tan, *Prog. Org. Coat.*, 2023, **174**, 107282.
- 58 W. Niu, G. Y. Chen, H. Xu, X. Liu and J. Sun, *Adv. Mater.*, 2022, **34**, 2108232.
- 59 H. Li, Y. Li, J. Wu, X. Jia, J. Yang, D. Shao, L. Feng, S. Wang and H. Song, *ACS Appl. Mater. Interfaces*, 2022, **14**, 29302–29314.
- 60 Y. Cheng, Y. Wang, X. Zhang, J. Zhang, Z. He, J. Wang and J. Zhang, *Nano Res.*, 2023, **16**, 7171–7179.
- 61 H. Ghasemi, G. Ni, A. M. Marconnet, J. Loomis, S. Yerci, N. Miljkovic and G. Chen, *Nat. Commun.*, 2014, **5**, 4449.
- 62 C. Chen, Y. Li, J. Song, Z. Yang, Y. Kuang, E. Hitz, C. Jia, A. Gong, F. Jiang, J. Y. Zhu, B. Yang, J. Xie and L. Hu, *Adv. Mater.*, 2017, **29**, 1701756.
- 63 N. Xu, X. Hu, W. Xu, X. Li, L. Zhou, S. Zhu and J. Zhu, *Adv. Mater.*, 2017, **29**, 1606762.
- 64 X. Wu, Y. Wang, P. Wu, J. Zhao, Y. Lu, X. Yang and H. Xu, *Adv. Funct. Mater.*, 2021, **31**, 2102618.
- 65 X. Lin, P. Wang, R. Hong, X. Zhu, Y. Liu, X. Pan, X. Qiu and Y. Qin, *Adv. Funct. Mater.*, 2022, **32**, 2209262.
- 66 Y. Zou, P. Yang, L. Yang, N. Li, G. Duan, X. Liu and Y. Li, *Polymer*, 2021, **217**, 123464.